JGR Biogeosciences

RESEARCH ARTICLE
10.1029/2026JG009856

Spatial and Temporal Patterns of Alkalinity in an Alpine Headwater Stream Network: Linking Catchment Heterogeneity to Carbon Dynamics

Francesco Presotto[1], Giulia Grandi[1,2], Rossano Piazza[1], Paolo Girardi[1], and Enrico Bertuzzo[1]

[1]Department of Environmental Sciences, Informatics and Statistics, University of Venice Ca' Foscari, Venice, Italy, [2]Ecole Polytechnique Fédérale de Lausanne, Lausanne, Switzerland

Key Points:

- Alpine stream alkalinity shows pronounced spatial heterogeneity
- Geological formations are identified as main drivers of spatial patterns of alkalinity
- Lateral inflows estimated for subcatchments predict network-scale alkalinity patterns

Correspondence to:
E. Bertuzzo,
enrico.bertuzzo@unive.it

Citation:
Presotto, F., Grandi, G., Piazza, R., Girardi, P., & Bertuzzo, E. (2026). Spatial and temporal patterns of alkalinity in an Alpine headwater stream network: Linking catchment heterogeneity to carbon dynamics. *Journal of Geophysical Research: Biogeosciences*, *131*, e2026JG009856. https://doi.org/10.1029/2026JG009856

Received 17 MAR 2026
Accepted 18 MAY 2026

Author Contributions:
Conceptualization: Francesco Presotto, Enrico Bertuzzo
Data curation: Francesco Presotto, Giulia Grandi
Formal analysis: Francesco Presotto
Investigation: Francesco Presotto
Methodology: Francesco Presotto, Rossano Piazza, Paolo Girardi, Enrico Bertuzzo
Supervision: Giulia Grandi, Enrico Bertuzzo
Validation: Paolo Girardi
Visualization: Francesco Presotto
Writing – original draft: Francesco Presotto, Enrico Bertuzzo
Writing – review & editing: Francesco Presotto, Giulia Grandi, Rossano Piazza, Paolo Girardi, Enrico Bertuzzo

Abstract Alkalinity is a key regulator of carbon dioxide (CO_2) dynamics in freshwater systems, influencing both dissolved inorganic carbon speciation and the buffering capacity of water. Despite its importance, alkalinity in freshwater environments remains comparatively underexplored relative to ocean systems. Here, we investigate alkalinity dynamics in an alpine stream network in the Dolomites (Italy) by sampling 15 sites at different temporal resolutions. Results indicate that alkalinity varies markedly across the network, ranging from approximately 1.9 to 4.3 mEq L^{-1}, whereas seasonal and diel fluctuations are less pronounced. By combining alkalinity and discharge measurements, we estimated the alkalinity of lateral inflows through a mass-balance approach and related it to catchment characteristics using a land use regression model, which identified three geological formations (Val Gardena sandstones, Gastropod Oolites Member, and Bellerophon Formation) as primary controlling factors, achieving an adjusted R^2 of 0.78 (cross-validated R^2 = 0.73). Furthermore, we propose a general framework for predicting in-stream alkalinity throughout the network by integrating the regression model with spatial estimates of lateral flow, providing a useful tool for studies of alkalinity and the related carbon dynamics in stream networks. Our findings underscore the importance of accounting for spatial variability in alkalinity when assessing carbon cycling in fluvial networks, particularly in mountain regions where geological features strongly influence carbon processing.

Plain Language Summary Streams and rivers are crucial components of the global carbon cycle because they transport and transform carbon as it moves from the land to the ocean. A key property controlling these processes is alkalinity, which determines how much carbon dioxide (CO_2) can be stored or released by water. In this study, we examined how alkalinity varies across a small (5 km^2) alpine stream network in the Dolomites (Italy). We measured alkalinity and streamflow at multiple sites and applied a mass balance model to estimate the alkalinity of water entering from the surrounding landscape. We found that alkalinity varies greatly from one stream to another, mainly because of differences in the types of rocks that the water flows through. In contrast, changes between seasons or between day and night were much smaller and less consistent. By linking field measurements with a modeling framework, we were able to map how alkalinity is distributed across the stream network. This approach helps explain how local geological and hydrological conditions shape stream chemistry and provides a useful tool for improving estimates of carbon dioxide fluxes and weathering-driven carbon storage in mountain regions.

1. Introduction

Total alkalinity (TA) is a fundamental regulator of ecological and biogeochemical processes occurring in natural waters. It is formally defined as the excess of proton acceptors over proton donors relative to a reference proton condition (Dickson, 1981; Wolf-Gladrow et al., 2007). In freshwater systems, carbonate species are typically the primary proton acceptors and total alkalinity can be approximated by

$$TA \approx TCA \approx \left[HCO_3^-\right] + 2\left[CO_3^{2-}\right] \quad (1)$$

where TCA is the total carbonate alkalinity. This simplified form reflects the dominance of bicarbonate (HCO_3^-) and, at higher pH, carbonate (CO_3^{2-}) ions in controlling alkalinity. Minor contributions from phosphate, silicate, sulfide, or organic acids may be relevant in nutrient-rich or specific environments, but in many conditions of

practical interest, carbonate species account for the overwhelming fraction of TA (Dickson, 1981; Wolf-Gladrow et al., 2007). Through its control on carbonate speciation, alkalinity regulates pH and is related to how dissolved inorganic carbon (DIC) is partitioned: DIC = $[CO_2]$ + $[HCO_3^-]$ + $[CO_3^{2-}]$, where CO_2 here represents both dissolved CO_2 and carbonic acid in water. By modulating carbonate equilibrium, alkalinity influences the partial pressure of CO_2 (pCO_2) in surface waters and thus the exchange of CO_2 with the atmosphere (Millero, 1995; Zeebe & Wolf-Gladrow, 2001). In high-alkalinity systems, buffering reactions shift DIC toward bicarbonate and carbonate ions, allowing substantial DIC transport in non-gaseous forms while sustaining CO_2 emissions during degassing (Duvert et al., 2019; Saccardi et al., 2024; Stets et al., 2017; Winnick & Saccardi, 2024). Consequently, alkalinity plays a central role in regulating carbon dynamics in riverine ecosystems. Alkalinity also interacts with stream metabolism (Battin et al., 2023). Gross primary production and ecosystem respiration (ER) alter CO_2 concentrations, and in systems with high alkalinity, carbonate buffering can dampen associated fluctuations in pH and DIC (Bernhardt et al., 2018; Bertagni et al., 2024; Saccardi et al., 2024; Shangguan et al., 2025). Thus, alkalinity not only reflects geochemical inputs but also modulates the expression of metabolic signals in CO_2 dynamics.

Alkalinity can be modified by specific biogeochemical processes. Although total alkalinity is conservative with respect to mixing, CO_2 atmospheric exchange and physical perturbations, it changes in response to reactions such as nitrification, calcification, and organic matter remineralization (Middelburg et al., 2020; Wolf-Gladrow et al., 2007). For instance, nitrogen fixation followed by nitrification constitutes a net TA sink, indirectly affecting CO_2 dynamics through acid–base interactions (Emerson & Hedges, 2008). Carbonate mineral reactions also strongly influence TA and CO_2 dynamics: precipitation of calcite removes alkalinity from the water column, whereas calcite dissolution releases alkalinity back. These processes regulate both TA and CO_2 fluxes by modulating carbonate buffering and DIC speciation. Recent modeling has demonstrated that calcite precipitation and dissolution are tightly coupled to stream metabolic dynamics and discharge variability (Diamond et al., 2025), highlighting their role in shaping CO_2 outgassing and alkalinity patterns in fluvial systems.

Despite its central role in regulating pH and carbon dynamics, alkalinity has been far more extensively studied in marine systems than in freshwater. Oceanographic research has established TA as a cornerstone variable for understanding carbonate chemistry and carbon–climate feedbacks, whereas in rivers and streams its spatial and temporal variability remains comparatively underexplored (Shangguan et al., 2025). Moreover, as highlighted by recent studies (Diamond & Bertuzzo, 2025; Rocher-Ros et al., 2025; Shangguan et al., 2024, 2025), accurate characterization of TA is needed for the correct interpretation of O_2–CO_2 data to jointly resolve stream metabolism and carbon fluxes, an emergent opportunity enabled by the increasing availability of CO_2 records at high temporal resolution. Recent modeling efforts (Shangguan et al., 2024) emphasize that without improved understanding of alkalinity variability in freshwaters, predictions of carbon cycling and climate feedbacks in fluvial networks remain highly uncertain.

This study addresses this knowledge gap by investigating temporal and spatial patterns of alkalinity in an alpine headwater stream network. We hypothesize that in alpine environments the heterogeneous combination of geology, elevation, and land cover can generate pronounced spatial gradients in alkalinity. This natural variability provides an ideal setting to investigate how catchment characteristics influence alkalinity and stream biogeochemistry. Although alpine and mountain streams cover a relatively small fraction of the global stream surface area, they play a crucial role in global carbon dioxide emissions due to their high CO_2 concentrations and gas reaeration rates (Horgby et al., 2019). Yet, constraining carbon cycling in these environments remains challenging, both because of their inherent heterogeneity and because data are comparatively scarce (Battin et al., 2023).

This study combines a mass balance approach with spatially and temporally resolved field measurements to investigate alkalinity dynamics. Particular attention was given to the characterization of lateral flow, as it represents a major input of solutes and water to the stream from surrounding hillslopes and groundwater sources. Lateral contributions are especially relevant in alpine catchments, where steep topography, shallow soils, and variable snowmelt patterns influence the timing, magnitude, and geochemical composition of incoming waters. We further explore through statistical modeling how catchment characteristics, such as geology, land cover, and elevation, influence these patterns. Finally, we propose a general approach to extrapolate alkalinity estimates from point measurements to the whole stream network, a feature that provides the foundation for future assessments of carbon dioxide (CO_2) fluxes and DIC dynamics in fluvial systems.

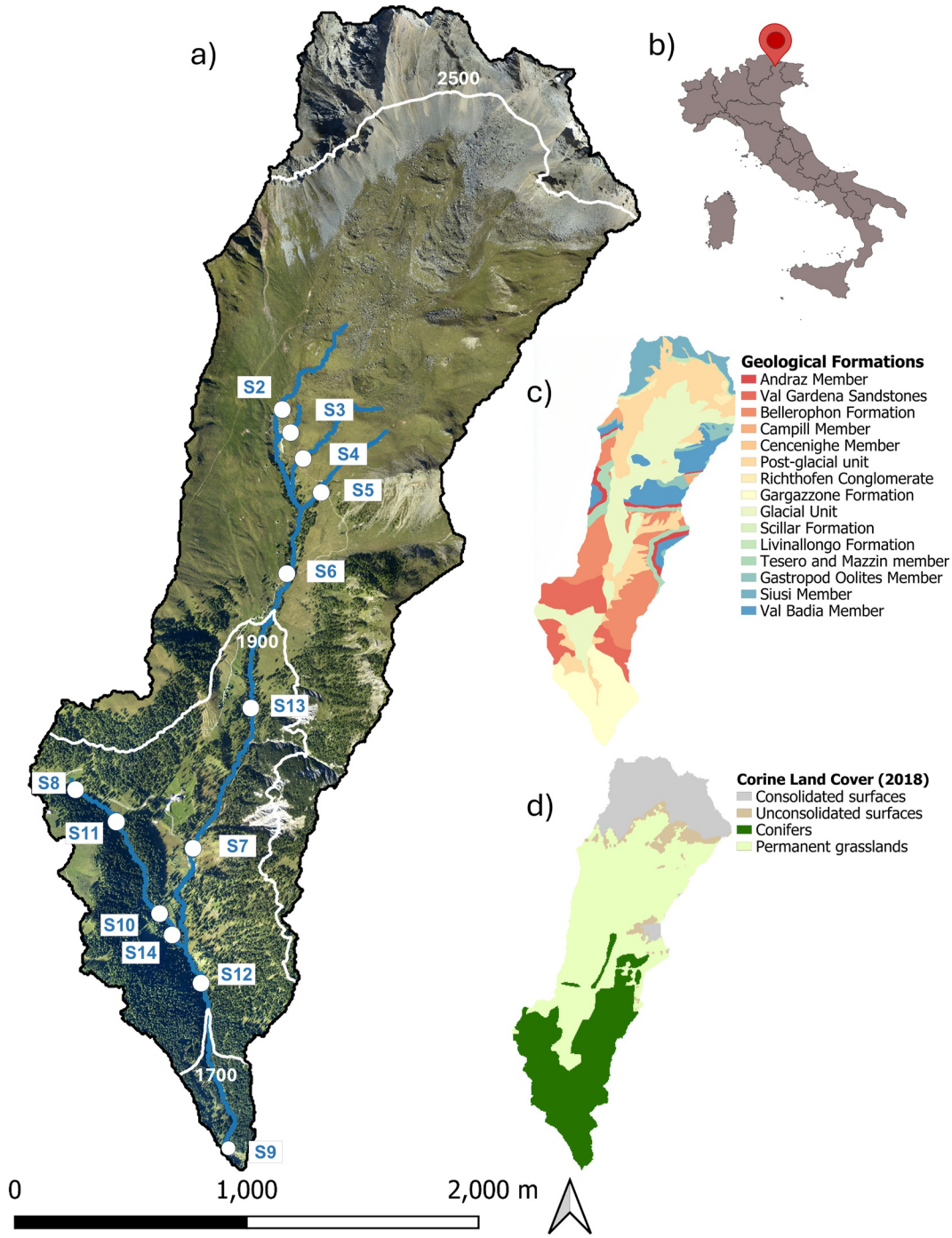

Figure 1. Overview of the Valfredda stream network. (a) Orthophoto of the catchment area illustrating the stream network (blue line) and the location of sampling sites S2–S14 (white dots). White contour lines indicate elevation (isoipses) in meters above sea level. (b) Catchment location: north-eastern Italian Alps. (c) Geological formations and members. (d) Corine Land Cover classes.

2. Methods

2.1. Site Description

The Valfredda stream network drains a 5.3 km^2 headwater catchment located in the eastern Italian Alps (Figure 1a). In the context of different research projects, extensive hydrological and geochemical data sets have

been gathered in the catchment since 2018 (Durighetto et al., 2020, 2025). The catchment spans elevations from 1,500 to 2,900 m above sea level, and its hydrologic regime is seasonally shaped by snow dynamics, exhibiting typical alpine features: cold, clear waters with high oxygen saturation. Continuous measurements at sites S7 and S11 showed dissolved oxygen ranging from 8 to 9.5 mg L^{-1} (97%–100% saturation, HOBO U26-001 Dissolved Oxygen Data Logger), water temperatures from 3°C in winter (December–February) to 11.5°C in summer (June–August) and specific conductivity that ranged from 200 µS cm^{-1} in S11 to a peak of 500 µS cm^{-1} at S7 and downstream points (HOBO U24-001 Fresh Water Conductivity Data Logger). Discharge is driven predominantly by summer storm events and spring (March–May) snowmelt, resulting in strong seasonal variability in flow and water temperature. The catchment has an alpine climate with an annual mean temperature of approximately 6–7°C and annual mean precipitation of about 1,500 mm. The wet season occurs mainly during spring and summer (March–August), while the dry season corresponds to winter (December–February), when the catchment is largely snow-covered.

Figure 1 highlights the spatial variability in lithological composition and land-cover types within the catchment. Land cover (Copernicus Land Monitoring Service, 2018) is characterized by a mosaic of sparse alpine vegetation, with high-elevation areas being dominated by scree slopes, bare rock, and alpine meadows (Figure 1d). Lower elevations support more continuous vegetation cover, including grasslands, shrublands, and patches of coniferous forest (primarily *Picea abies* and *Larix decidua*). Geologically, the catchment is characterized by a mosaic of carbonate- and silicate-rich lithologies. Carbonate-rich formations, including the Bellerophon Formation (BEL) and the Gastropod Oolites Member (OOL), are primarily located in the northern subbasins draining toward sites S4, S5, and S6, while the Val Gardena sandstones (AVG), a silicate-rich formation, dominate the central and southern subbasins feeding sites S8–S11 (Figure 1c). Glacial deposits and unconsolidated sediments overlay both carbonate and silicate units in certain areas, particularly along valley floors, influencing local lateral flow contributions (Abbà et al., 2018).

The river network was extracted from a 5 m digital terrain model by identifying source nodes at locations with the highest flow persistency, corresponding to perennial headwaters (Durighetto et al., 2020). Flow accumulation and flow direction were computed using the QGIS software to map the paths of water across the catchment. The information was used to establish connections between each pixel of the catchments and its downstream neighbors, thereby depicting the overall landscape connectivity. From this space-filling drainage network, the proper stream network was extracted by retaining only the pixels draining from identified spring or source locations. Each network node was then assigned attributes such as coordinates, elevation, drained area, upstream and downstream connections.

2.2. Alkalinity Sampling

The location of 13 sampling sites was selected to provide longitudinal coverage of the main stem (from S2 to S9, Figure 1a) and to include at least one site in each tributary. In some areas, the exact locations were constrained by accessibility and safety considerations. Alkalinity sampling was conducted using three complementary approaches: monthly grab sampling, targeted campaigns that include discharge measurements and high frequency sampling.

Monthly grab sampling was carried out at 10 sites (from S2 to S9 plus S11 and S12), distributed across the main stem and all tributaries, to capture spatial patterns and seasonal variability in total alkalinity (TA). The campaign lasted from 10 Jul 2024 to 18 Sep 2025 for a total of 110 samples. We additionally conducted four extensive field campaigns combining alkalinity and discharge measurements across the whole stream network (Table 1). This information allows, through a mass balance approach, a detailed reconstruction of alkalinity in lateral discharge. The four campaigns were conducted on 20 May 2025, 10 June 2025, 24 July 2025 and 18 September 2025 during spring-summer baseflow after the end of the snowmelt period. Days were selected based on accessible weather conditions and the absence of recent extreme events (e.g., storms or floods) to ensure safe fieldwork and representative baseflow conditions. Contextually, discharge was estimated through slug addition of saline solution at each sampling point. Finally, a 24-hour campaign was conducted at the catchment outlet (S9) where hourly samples were collected through an ISCO autosampler to investigate alkalinity diel variations. Samples were collected from 10-June-2025 at 11:30 to 11-June-2025 at 10:30, the same day of a targeted campaign. The information is also relevant to assess whether the time of the day of the targeted campaigns could have an effect on the alkalinity estimation.

Table 1
Measured Alkalinity (TA, meq L^{-1}, Shaded Columns) and Discharge (Q, L s^{-1}) at Each Sampling Point During the Four Targeted Field Campaigns

	May		June		July		September	
Sampling point	TA	*Q*	TA	*Q*	TA	*Q*	TA	*Q*
S2*	2.27	44.05	2.06	73.06	1.98	37.90	1.88	25.26
S3*	2.04	24.38	1.53	36.28	2.10	20.97	2.06	4.78
S4*	2.80	14.22	3.06	6.90	3.33	12.24	3.12	3.69
S5*	2.75	5.77	3.24	1.46	3.38	4.97	3.51	1.38
S6	2.37	100.16	2.21	118.8	2.26	86.1	2.34	52.60
S7	2.64	128.34	2.56	137.7	2.47	100.2	2.42	74.81
S8*	3.59	2.50	3.77	1.57	4.11	1.25	4.30	0.68
S9	2.60	175.97	2.52	205.53	2.73	172.4	–	–
S10	3.64	6.57	3.77	5.05	3.48	6.09	–	–
S11	3.81	4.85	4.07	3.68	4.00	2.80	4.31	1.96
S12	2.68	146.74	2.53	175.1	–	–	2.70	110.00
S13	–	–	–	–	–	–	2.35	53.12
S14	3.35	8.85	3.49	8.74	3.48	7.94	3.54	4.78

Note. Sampling points marked with an asterisk (*) indicate headwater sites with no other upstream sampling point. Site S13 was added only in the last campaign. Some measurements are missing due to time constrain during the field work.

Samples were collected in 50 mL Falcon® tubes, completely filled to prevent CO_2 exchange, kept cool during transport, and analyzed within the following 24 hr. Alkalinity was determined via titration following ISO 9963-1:1994, using a bromocresol-green/methyl-red mixed indicator and 0.01 mol L^{-1} HCl. The endpoint, corresponding to a pH of 4.6, yields total alkalinity (TA). To assess the precision of the method, we performed a 10-sample repetition test, which yielded an analytical uncertainty of ±0.04 mL of titrant, corresponding to ±0.01 mEq L^{-1}.

2.3. Land Use Regression for Alkalinity Prediction

As a preliminary step toward identifying the landscape features that control stream alkalinity, we use the data collected in the four targeted campaigns combined with a mass-balance approach to estimate the average alkalinity of the lateral discharge entering a portion of the stream network from its draining subcatchment. The oriented graph representation of the stream network implemented allows for the identification of the network area comprised between each sampling point and the upstream ones, defining the corresponding subcatchment. For instance, referring to Figure 1a, the subcatchment corresponding to site S12 is identified as the portion of catchment area that topographically drains into S12, after removing the contribution of closest upstream sites: S10 and S7. Note that the definition of a site subcatchment may vary between campaigns, depending on the availability of measurements at upstream sites (see Table 1). In all cases, the subcatchment characteristics (area, estimated lateral discharge and alkalinity, and related statistical features) were computed accordingly.

For a specific subcatchment identified by site i, the lateral discharge $Q_{L,i}$ can be derived as:

$$Q_{L,i} = Q_i - \sum_{j=1}^{N_u} Q_j, \tag{2}$$

where Q_i is the discharge measured at the site i and j denotes the set of immediately upstream points, up to N_u. Similarly, the average alkalinity of the lateral inflow, $TA_{L,i}$, can be obtained from a mass balance between the observed alkalinity flux at i and the contributions from its upstream sites:

$$TA_{L,i} = \frac{Q_i\, TA_i - \sum_{j=1}^{N_u} Q_j \cdot TA_{L,j}}{Q_{L,i}}. \tag{3}$$

This recursive formulation, applied at sampling point/subcatchment scale, ensures that lateral alkalinity computed for node i reflects only the processes and sources acting inside the i-the subcatchment. These calculations are performed for sites that have upstream sampling sites. For sites without upstream sampling locations (see Table 1, hereafter termed headwater sites), the measured discharge entirely represents lateral inputs from the local subcatchment, and the lateral alkalinity is thus by definition equal to the in-stream alkalinity observed at the site.

We then statistically relate $TA_{L,i}$ to the geological and land cover characteristics of the corresponding subcatchment. The underlying assumption is that alkalinity in lateral flow is primarily controlled by the soil, vegetation, and bedrock characteristics that infiltration water encounters along its hydrologic pathways. We focused on describing $TA_{L,i}$ rather than in-stream alkalinity (TA_i) dynamics to remove upstream–downstream dependencies. As such, observations of $TA_{L,i}$ can be considered independent and related only to the properties of the subcatchment i. We consider land cover (Copernicus Land Monitoring Service, 2018), geological composition (Abbà et al., 2018), and mean catchment elevation (Figure 1) as potential predictors. Specifically, we use the fraction of each subcatchment associated with different land-cover classes and geological types, for a total

of 20 possible predictors. As a preliminary step to the statistical analysis, we examined a Spearman correlation matrix between all candidate covariates to identify potential collinearity.

We adopt a mixed-effect linear regression model that is formally a Land Use Regression (LUR) approach (Beelen et al., 2013). While more complex model could be adopted, for example, generalized linear model, the linearity feature is key for the subsequent procedure of network interpolation, see below. As illustrated above, non-headwater sampling points may be subject to an additional source of error related to the computation of lateral alkalinity through Equations 2 and 3. To account for this, we grouped the data according to a headwater/non-headwater classification and included a random intercept as well as group-specific heteroskedastic variance of residuals. The general formulation of the linear mixed-effects model thus reads:

$$\mathrm{TA}_{\mathrm{L},ij} = \beta_0 + \sum_{k=1}^{p} \beta_k X_{k,ij} + b_{0j} + \varepsilon_{ij} \tag{4}$$

where $\mathrm{TA}_{L,ij}$ is the estimated lateral alkalinity at site i within group j, β_0 is the fixed intercept, β_k are the fixed-effect coefficients associated with the p predictors $X_{k,ij}$, $b_{0j} \sim \mathcal{N}(0, \sigma^2)$ is the random intercept associated with grouping factor j (headwater/non-headwater), and $\varepsilon_{ij} \sim \mathcal{N}(0, \tau_j^2)$ is the residual error term. All model terms in Equation 4, except the covariates $X_{k,ij}$ (which are dimensionless), are expressed in units of mEq L^{-1}.

Variable selection was implemented through a stepwise forward procedure. In the first stage, each predictor was fitted individually using model 4, corresponding to single-predictor models ($p = 1$). The fixed-effect coefficients β of each individual model were stored in order to consider the direction of the effect for the next steps. The predictor with the highest explanatory power (highest adjusted R^2) was selected as the starting covariate. In the second stage, the remaining candidate predictors were tested iteratively. At each step, a candidate predictor was added to the current model. A predictor was retained if: (a) it improved the adjusted R^2 by at least 1%; and (b) its estimated coefficient showed the same direction of effect as in the initial screening; otherwise, the predictor was excluded from the candidate list. Iterations stopped when no further variables could be added. This procedure ensured a parsimonious model that respected both explanatory power and plausibility, avoiding collinearity.

Finally, to evaluate the predictive performance and robustness of the selected LUR model, we applied a leave-one-out cross-validation (LOOCV) procedure. For each iteration, one observation was excluded from model fitting and subsequently predicted using the model calibrated on the remaining data. The overall performance was then quantified by comparing the cross-validated predictions against the observed values.

2.4. Network-Scale Pattern of Alkalinity

Based on the results of the LUR model, we outline a general procedure to interpolate stream alkalinity at every node of the network, that is, for each pixel classified as a channel during the extraction of the network from the digital elevation model. In short, the procedure consists of applying the same recursive mass-balance approach described above to derive lateral alkalinity, but in reverse order. For each network node i, in-stream alkalinity is computed by combining the contributions from all immediately upstream nodes with the local lateral input from the portion of the catchment draining directly into i. Specifically, TA_i is defined as the ratio between the alkalinity mass flux and the discharge flowing through i:

$$\mathrm{TA}_i = \frac{\sum_{j=1}^{N_u} Q_j \cdot \mathrm{TA}_j + Q_{L,i} \cdot \mathrm{TA}_{\mathrm{L},i}}{\sum_{j=1}^{N_u} Q_j + Q_{\mathrm{L},i}}, \tag{5}$$

To compute the lateral discharge, we assumed that the specific lateral discharge (i.e., discharge per unit area), estimated at the subcatchment scale using Equation 2, applies uniformly to all pixels within the subcatchment. We estimated $\mathrm{TA}_{\mathrm{L},i}$ with the selected regression model, based on local catchment characteristics. Indeed, the linearity of the model allows its application at any arbitrary spatial scale while preserving the average value, which physically translates into alkalinity mass conservation. This approach ensures that in-stream alkalinity reflects both the cumulative contributions from upstream nodes and the lateral inputs from the local subcatchment, providing a spatially explicit prediction across the river network.

The procedure outline above, however, can quickly become cumbersome and time-consuming. The reason is twofold: first, Equation 5 has to be computed recursively from upstream to downstream; second, the covariates of the statistical model must be computed for every single network node (approximately 1200 in this particular application). A more efficient strategy is to apply the model directly to all pixels within the catchment and carry out the computations using matrix operations as detailed in the following. Similarly to Equation 5, the mass flux of alkalinity ϕ_i flowing through the generic pixel i of the catchment is governed by the mass balance:

$$\phi_i = \sum_{j=1}^{N} W_{ji}\phi_j + \sum_k \beta_k X_{ki}\, q_{\mathrm{L},i}\, a \tag{6}$$

where N is the total number of pixels in the catchment; W_{ij} is an element of the connectivity matrix $\boldsymbol{W}$, with $W_{ij} = 1$ if the pixel i drains into j and $W_{ij} = 0$ otherwise; X_{ki} denotes the k-th model covariate for the pixel i and β_k is the corresponding coefficient; and a represents the area of a pixel.

Defining the column vector $\boldsymbol{\phi} = (\phi_1, \phi_2, \ldots, \phi_N)^T$ (superscript T indicates matrix transposition), and analogously $\boldsymbol{q}_\mathrm{L}$ and $\boldsymbol{\beta}$, Equation 6 can be written in matrix form as

$$\boldsymbol{\phi} = \left(\boldsymbol{W}^T\boldsymbol{\phi} + \boldsymbol{X\beta} \odot \boldsymbol{q}_\mathrm{L}\right), \tag{7}$$

where $\odot$ indicates the Hadamard element-wise product. Equation 7 can directly be solved as:

$$\boldsymbol{\phi} = \left(\boldsymbol{I} - \boldsymbol{W}^T\right)^{-1}\boldsymbol{X\beta} \odot \boldsymbol{q}_\mathrm{L}, \tag{8}$$

where $\mathbf{I}$ is the identity matrix. Analogously, discharge flowing in each pixel reads:

$$\boldsymbol{Q} = \left(\boldsymbol{I} - \boldsymbol{W}^T\right)^{-1}\boldsymbol{q}_\mathrm{L}\, a, \tag{9}$$

Finally, stream alkalinity is derived by element-wise division between $\boldsymbol{\phi}$ and $\mathbf{Q}$ for the pixels classified as channel.

3. Results

3.1. Spatial and Temporal Dynamics of Alkalinity

Alkalinity in the Valfredda catchment shows strong heterogeneity across the stream network and a comparatively low seasonal variability (Figure 2a). At the seasonal scale (Figure 2a), it is possible to identify a mild temporal pattern with alkalinity peaking in late winter to early spring (February–April) and reached minimum values in summer (June–August). This pattern is more evident at downstream sites (S7 and S9), though the magnitude and variability differed among locations. Data gaps occurred at some high-elevation sites (from S2 to S5) due to snow cover and freezing conditions that prevented winter sampling.

At the diel scale (Figure 2b), 24-hour measurements from June 10–11 2025 at the catchment outlet (S9), showed modest fluctuations (2.51–2.61 mEq L^{-1}) without a systematic day–night pattern. A slight afternoon peak around 15 and another around 22 was followed by an immediate decline and stabilization. Data were collected on the same day of a targeted campaign across the entire network (June 10–11, 2025). In these campaigns, samples from the different sites are typically collected between 10:00 and 17:00. As the outlet integrates the signal from the entire network, we can assume that the absence of a significant diel pattern also applies to a large part of the studied system. This suggests that sampling time has a negligible effect on the observations and that the snapshot provided by the targeted campaigns is representative of the spatial pattern of alkalinity during baseflow. However, we cannot exclude the possibility that small headwaters, whose contribution to the signal at the outlet is almost negligible, exhibit diel fluctuations.

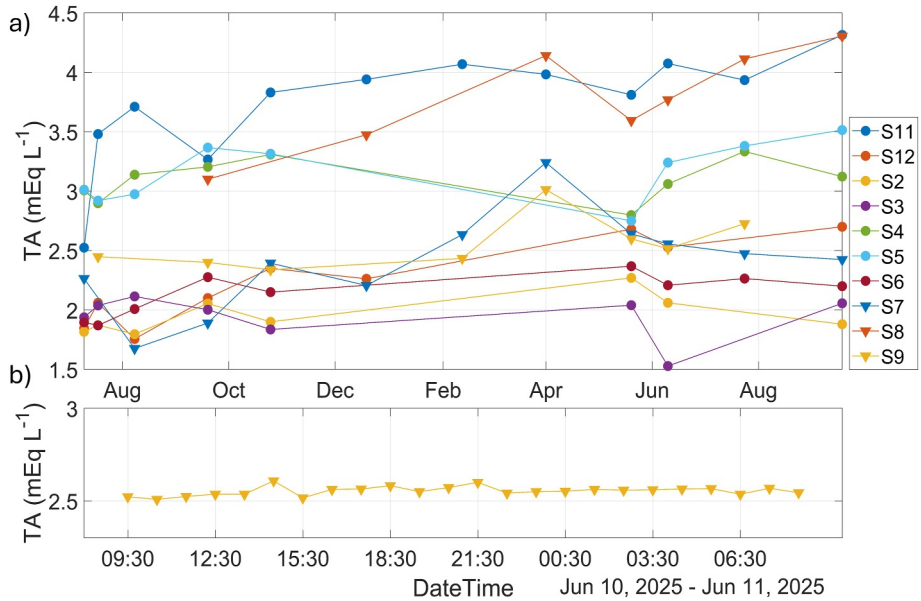

Figure 2. Temporal variability of TA (mEq L^{-1}): (a) Seasonal dynamics across stream sites from July 2024 to September 2025. To improve readability, only stations with at least four samples are displayed; gaps reflect access limitations during snow and ice. (b) Diel dynamics from autosampler measurements on June 10–11, 2025, showing minimal variation and no clear day–night cycle (the *y*-axis spans the range of values observed at the station).

3.2. Predictors of Lateral Alkalinity From LUR Analysis

Prior to model fitting, correlation among all candidate predictors were evaluated using a Spearman rank correlation analysis (Figure 3). The matrix reveals widespread and often strong collinearity among several geological units (e.g., Campill Member and glacial deposits), consolidated and unconsolidated surface classes, and land cover variables. In addition, mean sub-basin altitude exhibits high correlations with both geological and vegetation-related predictors, reflecting the strong elevation control on lithological exposure and land use distribution in the catchment. Statistically significant correlations ($p < 0.05$, bold values) frequently exceed conventional thresholds for multicollinearity concern. This pattern reinforces the necessity of the variable selection strategy implemented in the LUR framework to mitigate multicollinearity issues.

The estimated lateral alkalinity inputs (Figure 4a) further illustrate the spatial heterogeneity of alkalinity sources across subbasins. Subcatchments in the northern part, especially those draining toward S4 and S5, exhibit relatively high TA_L, consistent with the elevated in-stream concentrations observed in their receiving reaches. Similarly, the subbasins feeding into the S8 branch show decreasing TA_L values downstream, reflecting the decline in in-river alkalinity along this branch. By contrast, in the southern part of the catchment, lateral alkalinity inputs appear weaker, suggesting reduced fluxes from surrounding hillslopes. A preliminary comparison of observed TA_L variance between headwater and non-headwater sites did not reveal significant differences (*F*-test: $F = 1.53, p = 0.36$). To quantitatively explain these spatial patterns, we applied the LUR framework. All tested predictors and their contributions to model R^2 at each step of the iterative procedure are reported in Table 2. The final model retained three geological predictors: Val Gardena sandstones (AVG), Gastropod Oolites Formation (OOL) and Bellerophon Formation (BEL). The model showed highly significant ($p < 0.001$) and positive (AVG: 2.67, OOL: 7.88, BEL: 3.24) coefficients for all three selected predictors and a adjusted R^2 of 0.78 (Table 3, Figure 4b). The estimated standard deviation of the random intercept was very limited (std = 4.04×10^{-6}). As a sensitivity analysis, we run a model selection without a random intercept term which yielded comparable results. On the other hand, residual variance differed significantly between headwater and non-headwater groups, with non-headwater residuals showing higher variance (0.18 vs. 0.06; $p = 0.027$). Performance was consistent across the two groups (Figure 4b), although errors were lower in headwater sites (RMSE = 0.28, $n = 20$) compared to non-headwater sites (RMSE = 0.47, $n = 20$).

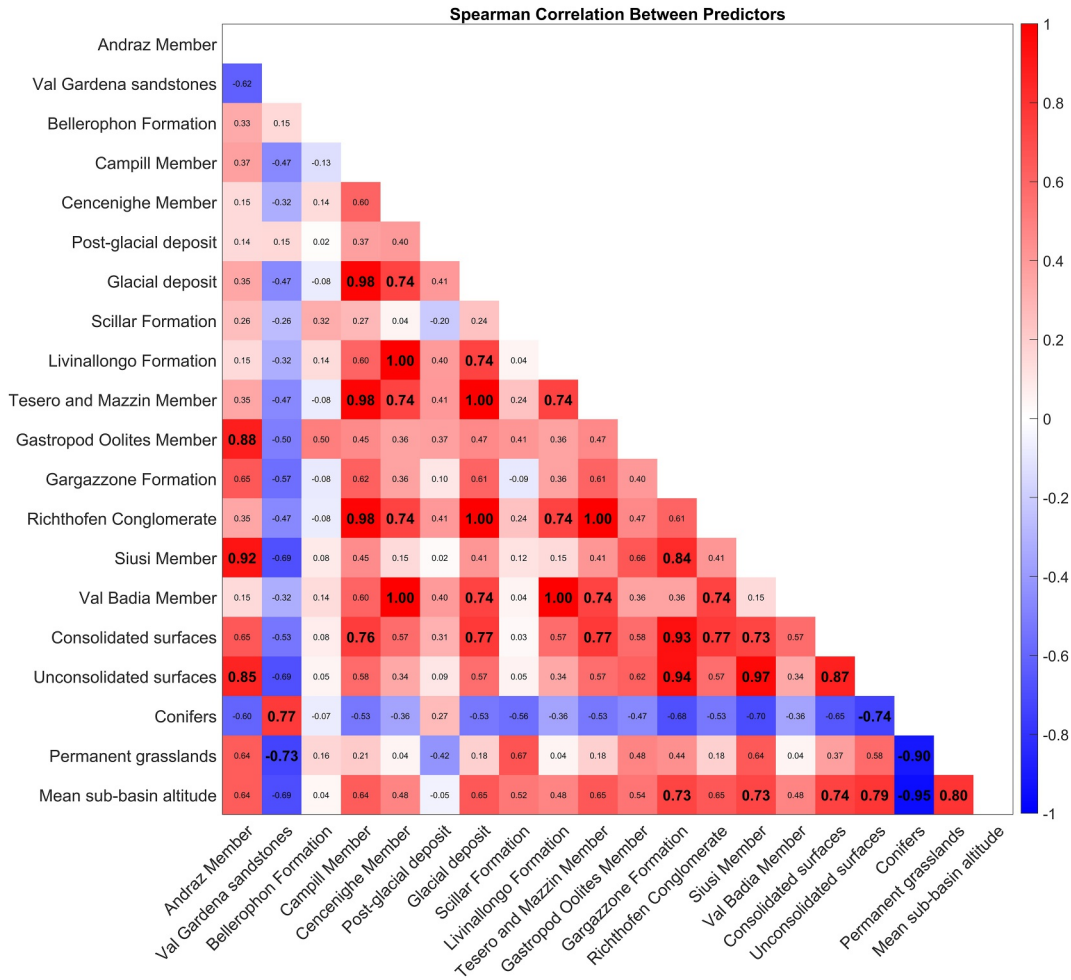

Figure 3. Spearman correlation matrix among all candidate predictors used in the Land Use Regression analysis. Bold values indicate statistically significant correlations ($p < 0.05$).

To assess the robustness of the selected LUR model, we further conducted a leave-one-out cross-validation (LOOCV) test. The LOOCV results confirm the model's strong predictive skill, with an overall $R^2_{CV} = 0.73$, a root mean square error (RMSE) of 0.39, a mean absolute error (MAE) of 0.31, and a negligible bias (−0.002). The negligible bias indicates that predictions are not systematically over- or under-estimated.

3.3. River Network Predicted Alkalinity

The LUR-derived predictions of lateral alkalinity were propagated across the stream network using the recursive mass balance approach described in subsection 2.4. This allowed us to generate spatially explicit profiles of in-stream alkalinity by integrating heterogeneous lateral flow and lateral alkalinity with upstream fluxes (Figure 5). The resulting profiles reveal distinct spatial patterns. Along the main stem, in-stream alkalinity shows a mild but progressive increase in the downstream direction, while tributary originating at S8 exhibits a decreasing trend downstream. In the upper part of the catchment, the tributaries corresponding to sites S4 and S5 display relatively high alkalinity concentrations close to their sources due to the drainage of landscape areas dominated by the Gastropod Oolites Member, which, according to the estimated model, contributes to enhanced lateral alkalinity. However, the strong longitudinal gradients are likely unrealistic and highlight a possible limitation of the model, as discussed in Section 4.5.

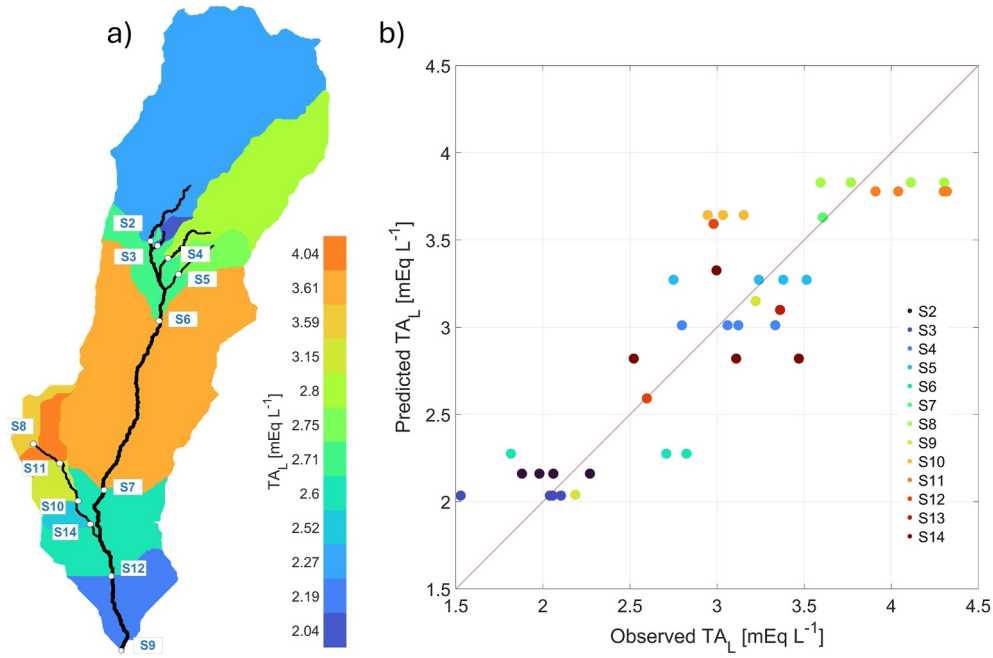

Figure 4. (a) Estimated TA_L inputs for each subcatchment for the 20th May 2025 campaign. (b) Predicted TA_L obtained from the Land Use Regression model plotted against TA_L estimated from data of all 4 targeted campaigns. Each site has multiple observed TA_L values, one for each targeted campaign, while the corresponding predicted value is the same for model construction. The 1:1 reference line is plotted in red.

4. Discussion

4.1. Temporal Variability of Stream Alkalinity

This study shows that alkalinity, both in lateral flow and in-stream, can exhibit high spatial heterogeneity in an alpine headwater catchment, primarily linked to the distribution of catchment lithology. Seasonal hydrological variability, however, did not induce a consistent pattern across all sites, and temporal fluctuations were generally modest, though some reaches experienced more pronounced changes. Catchment hydrology can control alkalinity, and more in general hydrochemistry, via the water transit time, defined as the time water spends traveling through the catchment before reaching the stream, because it determines the contact time between water and reactive minerals (Druhan & Benettin, 2023). Higher groundwater contributions, which typically involve longer transit times, are expected to increase alkalinity, whereas shorter hydrological pathways associated with rainfall-induced flow may lead to lower alkalinity (Bernal et al., 2022). However, this expected relationship could not be clearly identified in the present case study, as hydrological dynamics are largely dominated by groundwater flow and sampling was conducted mainly under baseflow conditions, far from the short and infrequent flow events characteristic of this catchment.

Hydrological processes can also generate diel cycles in stream alkalinity through similar mechanisms. High daytime evapotranspiration can enhance groundwater contributions relative to interflow, resulting in higher alkalinity concentrations during the day (Shangguan et al., 2021; Wilcock & Chapra, 2005). Conversely, in highly productive streams, primary producers can induce an opposite pattern by using calcification, which consumes alkalinity, as a source of inorganic carbon (Diamond et al., 2025). Both processes are likely minimal in the Valfredda catchment, where the alpine climate limits evapotranspiration and stream productivity is low. Consistent with this expectation, we observed no diel alkalinity cycle at the catchment outlet (S9). Because this site integrates upstream contributions from the entire river network, the observed pattern likely reflects the aggregated catchments response. However, we acknowledge that small headwaters, which exert a relatively small influence on outlet alkalinity, could potentially exhibit slightly different diel variability.

Table 2
Iterative Procedure for Model Selection

	Start		Step 1		Step 2		Step 3	
Model	R^2	β	R^2	β	R^2	β	R^2	β
Andraz Member	0.019	−3.18	0.456	2.29	0.675	5.97	0.786	2.78*
Val Gardena sandstones	**0.447**	**1.90**	–	–	–	–	–	–
Bellerophon Formation	0.046	1.68	0.507	1.91	**0.784**	**3.24**	–	–
Campill Member	0.081	−32.2	0.448	−1.33	0.630	−11.9	0.776	−2.02
Cencenighe Member	0.185	−1618	0.513	−1003	0.641	−577	0.779	−239
Post-glacial deposit	0.053	−0.95	0.512	−1.05	0.646	−0.68	0.783	−0.36
Glacial deposit	0.134	−0.99	0.469	−0.62	0.595	−0.22	0.752	0.13
Sciliar Formation	0.185	−9474	0.487	−5874	0.611	−3379	0.754	−1397
Livinallongo Formation	0.184	−55.7	0.476	−32.1	0.611	−19.6	0.753	−7.70
Tesero and Mazzin Member	0.030	−2.22	0.420	0.61	0.639	3.13	0.760	1.45
Gastropod Oolites Member	0.009	1.27	**0.621**	**6.02**	–	–	–	–
Gargazzone Formation	0.034	−0.76	0.429	−0.43	0.590	6.00	0.750	7.93
Richthofen Conglomerate	0.185	−5.44	0.484	−3.32	0.611	−1.94	0.754	−0.79
Siusi Member	0.008	0.26	0.583	1.30	0.591	0.32	0.750	−0.11
Val Badia Member	0.185	−1087	0.487	−674	0.611	−388	0.754	−160
Consolidated surfaces	0.177	−2.01	0.465	−1.07	0.606	−0.64	0.753	−0.26
Unconsolidated surfaces	0.012	−1.73	0.554	6.29	0.626	−2.68	0.778	−1.72
Conifers	0.205	0.78	0.470	−0.44	0.621	−0.06	0.776	−0.07
Permanent grasslands	0.124	−0.70	0.493	0.62	0.629	0.27	0.778	0.15
Mean sub-basin altitude	0.198	−0.01	0.448	0.00	0.634	−0.01	0.777	0.00

Note. R^2 Values From the Land Use Regression Model and Corresponding β Coefficients for Each Covariate. **Bold** values indicate the predictor selected at each step and subsequently removed in the following steps. The LME model evaluated at each step includes the previously selected predictors plus the one being tested. Model selection stopped at step 2 (3 predictors). Indeed at step 3, the sign of the β coefficient for the predictor with the highest R^2 (indicated with the asterisk) reversed its sign with respect to the initial evaluation (start).

4.2. Geological Controls on Lateral Alkalinity Inputs

While temporal variability was limited under baseflow conditions, spatial variability in alkalinity was pronounced and largely explained by geology. Carbonate-rich units such as the Bellerophon Formation and the Gastropod Oolites Member strongly promoted alkalinity generation, while the Val Gardena sandstones exerted a weaker but still positive effect. The high collinearity among several geological, surface, and vegetation predictors (Figure 3) justified the use of a LUR framework with stepwise selection, which allowed us to identify a parsimonious and physically meaningful set of predictors while reducing redundancy and ensuring stable parameter estimates (Beelen et al., 2013). These relationships highlight the dominant role of lithological controls in shaping lateral alkalinity sources, consistent with the view that carbonate weathering is a primary driver of stream buffering capacity (Lauerwald et al., 2015). Geology could also indirectly influence transit times, since lithological differences in permeability and storage regulate how long water interacts with reactive substrates before reaching the stream (Benettin et al., 2022). The LUR model did not identify a clear influence of land cover, while other studies found that vegetation can enhance bicarbonate solubilization in riverine ecosystems (Lehmann et al., 2023). This suggests that geological heterogeneity outweighs vegetation effects in this alpine setting.

Table 3
Results of the Land Use Regression Model Using LME With Group-Specific Variances

Predictor	Estimate ± SE	Adjusted R^2
Intercept (β_0)	2.03 ± 0.11***	–
Val Gardena sandstones (AVG)	2.67 ± 0.25***	0.447
Gastropod Oolites Member (OOL)	7.88 ± 1.20***	0.621
Bellerophon Formation (BEL)	3.24 ± 0.65***	0.784

Note. The table reports parameter estimates (± standard error), with asterisks indicating levels of statistical significance. The progressive increase in adjusted R^2 is shown as covariates are added sequentially. $^{*}p < 0.05$; $^{**}p < 0.01$; $^{***}p < 0.001$.

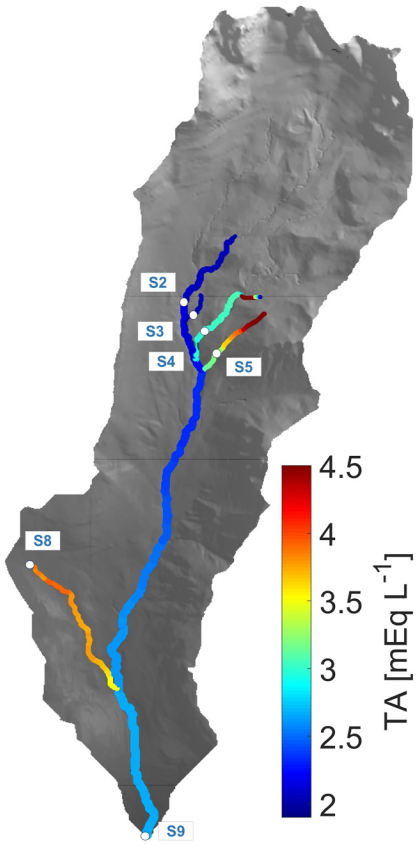

Figure 5. Spatial distribution of alkalinity in the study catchment. Predicted in-stream TA obtained from the Land Use Regression model applying the mass balance-approach. Lateral discharge data refers to the May sampling, representative of the spring-summer baseflow. White dots refer to the headwater and outlet stations.

4.3. Network-Scale Propagation of Alkalinity

Building on these spatially explicit estimates of lateral alkalinity inputs, we propagated alkalinity across the river network using a mass balance framework. The resulting longitudinal patterns reflect both upstream inheritance and local inputs. Along the main stem, alkalinity progressively increases downstream. Conversely, the S8 tributary shows a decreasing downstream trend, consistent with weaker lateral inputs from its subcatchments. Tributaries draining toward S4 and S5 display relatively high concentrations near their sources, which are progressively diluted along the flow path. These patterns underscore how heterogeneous subcatchments imprint distinct signatures on network-scale alkalinity dynamics. Stream network confluences have been identified as potential hotspots of biogeochemical activity due to the mixing of waters with distinct biogeochemical signatures (Lupon et al., 2025). The results presented here indicate that confluences can also promote sharp spatial variations in alkalinity, with relevant implications for the carbonate equilibrium and, consequently, for the relative availability of different inorganic carbon species to aquatic organisms.

In addition to the specific insights gained from the Valfredda stream network, the proposed framework is inherently general and can be readily adapted to other catchments or study contexts. By combining statistical inference of lateral alkalinity from geology with explicit network-scale mass balance modeling, we provide a transferable approach for linking point measurements to catchment-wide dynamics. To address this task, namely, deriving network-scale estimates from point measurements, a commonly used approach in the literature is the Spatial Stream Network model (Dumelle et al., 2024). This method performs regression and prediction based on network-defined covariance structures while accounting for spatial autocorrelation and error propagation along the stream network, making it a valuable tool in many hydrological and ecological applications. The advantages of the method proposed in this specific case study lies in its explicit representation of the role of lateral contributions in controlling in-stream alkalinity, grounded in a physically based alkalinity mass balance that satisfies the principle of mass conservation. Moreover, the network structure is explicitly incorporated through the recursive routing of lateral flow and alkalinity from upstream to downstream segments.

4.4. Implications for Carbon Cycling and Modeling Frameworks

Our analysis shows that alkalinity cannot be treated as a constant property even within small catchments. Both spatial and temporal variability can be substantial, driven by geological heterogeneity, hydrological dynamics, and seasonal forcing. This has major implications, as alkalinity governs stream buffering capacity and directly regulates the amount of DIC present as CO_2 and available for exchange with the atmosphere. Coarse-resolution alkalinity estimates are commonly used to quantify inland water CO_2 fluxes at large scales (Raymond et al., 2013), but our results emphasize that high-resolution approaches are essential for capturing fine-scale drivers of carbon cycling. Without targeted measurements or an appropriate modeling framework, these variations will remain hidden, leading to biased estimates of carbon fluxes and misrepresentation of catchment-scale processes.

A growing body of recent research (Diamond & Bertuzzo, 2025; Rocher-Ros et al., 2025; Shangguan et al., 2024, 2025) emphasizes that quantification of total alkalinity (TA) is essential to correctly interpret O_2–CO_2 relationships and to improve estimates of stream metabolism and carbon fluxes. Our results suggest that not only the value of total alkalinity (TA) should be considered, but also its potential longitudinal gradients. Neglecting these variations may lead to biased estimates when applying single- or two-station approaches (Shangguan et al., 2024). The longitudinal patterns of alkalinity derived from the proposed framework can be directly incorporated into one-dimensional models of stream DIC cycling, as proposed in Dolcetti et al. (2025) and Saccardi et al. (2024).

Understanding alkalinity conditions in stream networks is also fundamental for assessing the contribution of rock weathering to the long-term carbon balance (Amiotte Suchet et al., 2003; Maher & Chamberlain, 2014). In this context, disentangling the relative roles of geology and hydrology is key to this goal: the pronounced spatial gradients highlighted here, together with the chemostatic behavior widely observed for weathering-derived solutes (Godsey et al., 2009), suggest that lithological heterogeneity primarily controls alkalinity concentrations, at least under baseflow or mild flow conditions. Whether this relative importance holds also during stormflows, when rapid hydrological pathways may bypass reactive substrates, remains an open question for future work. In a related perspective, carbon dioxide removal strategies based on enhanced weathering are gaining increasing attention (Gaucher et al., 2025; Köhler et al., 2016). When applied on land, these approaches increase the alkalinity of downstream river networks, highlighting the need for robust frameworks capable of quantifying both baseline and enhanced alkalinity, particularly in mountainous and carbonate-rich regions (Regnier et al., 2022; Rocher-Ros et al., 2025).

4.5. Limitations and Future Directions

Some limitations of the current model formulation should also be acknowledged. First, the mass-balance approach used to estimate lateral alkalinity is applicable only to stream segments that are gaining water. In losing reaches, where water flows from the stream into the subsurface, lateral alkalinity cannot be estimated. Under such conditions, lateral alkalinity does not influence in-stream alkalinity, and thus this limitation is not critical per se. However, when a stream reach includes alternating gaining and losing segments, neglecting this spatial heterogeneity may lead to an overestimation of lateral inputs. Second, our framework currently considers only the lithology traversed by water, without explicitly accounting for transit times. Because longer water residence within a given rock unit typically enhances solute mobilization and weathering, incorporating transit time could refine predictions of alkalinity generation and improve the representation of temporal dynamics. Addressing these limitations in future work would enhance the accuracy and generality of network-scale alkalinity modeling. The assumption of linearity allows the model to be applied across different spatial scales. We exploited this property to use parameters estimated from subcatchment-scale lateral alkalinity data to derive alkalinity at the pixel scale along the stream network (Figure 5). However, near stream sources, where alkalinity is largely controlled by local lateral inputs, this approach may introduce some artifacts, such as the pronounced gradients in predicted instream alkalinity observed in the tributaries draining into S4 and S5. This limitation becomes less relevant in downstream sections with larger drainage areas, where spatial averaging of covariates yields more statistically representative values. Therefore, predictions for stream sections with small drainage areas dominated by a few or a single geological formations should be interpreted with caution.

Despite these limitations, the framework presented here provides a robust basis for future studies. By explicitly linking local lithological controls with network-scale mass balance, it offers a transferable approach not only for modeling alkalinity but also for investigating other solutes and biogeochemical processes, including in-stream CO_2 dynamics, that depend on spatially variable alkalinity. As such, this approach can serve as a reference for field-based and modeling studies aiming to capture the coupled effects of hydrology, geology, and biogeochemistry in alpine stream networks.

Acknowledgments
EB and GG gratefully acknowledge the support provided by the European Union through the Next-GenerationEU plan: PNRR–M.4 C.2, INVESTIMENTO 1.1: Programma Nazionale di Ricerca e Progetti di Rilevante Interesse Nazionale (PRIN), Project: CONSTRAIN - CarbON exchange processes across STReAm INterfaces, code: 20223XTPK7, CUP: H53D23001420006. This manuscript reflects only the Authors views and opinions, neither the European Union nor the European Commission can be considered responsible for them. This work took place within the framework of the DoE 2023–2027 (MUR, AIS.DIP. ECCELLENZA2023_27.FF project). Open access publishing facilitated by Universita Ca' Foscari, as part of the Wiley - CRUI-CARE agreement.

Conflict of Interest

The authors declare no conflicts of interest relevant to this study.

Availability Statement

Data presented in this study are available in the public repository: https://zenodo.org/records/17434517.

References

Abbà, T., Breda, A., Massironi, M., Preto, N., Piccin, G., Trentini, T., et al. (2018). Pre-Alpine and Alpine deformation at San Pellegrino pass (Dolomites, Italy). *Journal of Maps*, *14*(2), 671–679. https://doi.org/10.1080/17445647.2018.1536001

Amiotte Suchet, P., Probst, J.-L., & Ludwig, W. (2003). Worldwide distribution of continental rock lithology: Implications for the atmospheric/soil CO_2 uptake by continental weathering and alkalinity river transport to the oceans. *Global Biogeochemical Cycles*, *17*(2). https://doi.org/10.1029/2002GB001891

Battin, T. J., Lauerwald, R., Bernhardt, E. S., Bertuzzo, E., Gener, L. G., Hall Jr, R. O., et al. (2023). River ecosystem metabolism and carbon biogeochemistry in a changing world. *Nature*, *613*(7944), 449–459. https://doi.org/10.1038/s41586-022-05500-8

Beelen, R., Hoek, G., Vienneau, D., Eeftens, M., Dimakopoulou, K., Pedeli, X., et al. (2013). Development of NO_2 and NO_x land use regression models for estimating air pollution exposure in 36 study areas in Europe – The escape project. *Atmospheric Environment*, *72*, 10–23. https://doi.org/10.1016/j.atmosenv.2013.02.037

Benettin, P., Rodriguez, N. B., Sprenger, M., Kim, M., Klaus, J., Harman, C. J., et al. (2022). Transit time estimation in catchments: Recent developments and future directions. *Water Resources Research*, *58*(11), e2022WR033096. https://doi.org/10.1029/2022WR033096

Bernal, S., Cohen, M. J., Ledesma, J. L., Kirk, L., Martí, E., & Lupon, A. (2022). Stream metabolism sources a large fraction of carbon dioxide to the atmosphere in two hydrologically contrasting headwater streams. *Limnology and Oceanography*, *67*(12), 2621–2634. https://doi.org/10.1002/lno.12226

Bernhardt, E. S., Blaszczak, J. R., Ficken, C. D., Fork, M. L., Kaiser, K. E., & Seybold, E. C. (2018). Metabolic regimes in rivers: Daily variability and controls on CO_2 fluxes. *Limnology and Oceanography Letters*, *3*(3), 89–100. https://doi.org/10.1002/lol2.10060

Bertagni, M. B., Regnier, P., Yan, Y., & Porporato, A. (2024). A dimensionless framework for the partitioning of fluvial inorganic carbon. *Geophysical Research Letters*, *51*(19), e2024GL111310. https://doi.org/10.1029/2024GL111310

Copernicus Land Monitoring Service. (2018). *Copernicus land monitoring service*. European Environment Agency (EEA).

Diamond, J. S., & Bertuzzo, E. (2025). A coupled O_2-CO_2 model for joint estimation of stream metabolism, O-C stoichiometry, and inorganic carbon fluxes. *Journal of Geophysical Research: Biogeosciences*, *130*(4), e2024JG008401. https://doi.org/10.1029/2024JG008401

Diamond, J. S., Truong, A. N., Abril, G., Bertuzzo, E., Chanudet, V., Lamouroux, R., & Moatar, F. (2025). Inorganic carbon dynamics and their relation to autotrophic community regime shift over three decades in a large, alkaline river. *Limnology and Oceanography*, *70*(5), 1122–1136. https://doi.org/10.1002/lno.70016

Dickson, A. (1981). An exact definition of total alkalinity and a procedure for the estimation of alkalinity and total inorganic carbon from titration data. *Deep-Sea Research, Part A: Oceanographic Research Papers*, *28*(6), 609–623. https://doi.org/10.1016/0198-0149(81)90121-7

Dolcetti, G., Piccolroaz, S., Bruno, M. C., Calamita, E., Larsen, S., Zolezzi, G., & Siviglia, A. (2025). Quantification of carbopeaking and CO_2 fluxes in a regulated alpine river. *Water Resources Research*, *61*(2), e2024WR037834. https://doi.org/10.1029/2024WR037834

Druhan, J. L., & Benettin, P. (2023). Isotope ratio–discharge relationships of solutes derived from weathering reactions. *American Journal of Science*, *323*. https://doi.org/10.2475/001c.84469

Dumelle, M., Peterson, E. E., Ver Hoef, J. M., Pearse, A., & Isaak, D. J. (2024). SSN2: The next generation of spatial stream network modeling in R. *Journal of Open Source Software*, *9*(99), 6389. https://doi.org/10.21105/joss.06389

Durighetto, N., Britt, R., Schirmer, M., & Botter, G. (2025). Variability in the shape of the active length–streamflow relationship in temporary streams: Insights from an empirical analysis. *Water Resources Research*, *61*(6), e2024WR038732. https://doi.org/10.1029/2024WR038732

Durighetto, N., Vingiani, F., Bertassello, L. E., Camporese, M., & Botter, G. (2020). Intraseasonal drainage network dynamics in a headwater catchment of the Italian Alps. *Water Resources Research*, *56*(4), e2019WR025563. https://doi.org/10.1029/2019WR025563

Duvert, C., Hutley, L. B., Beringer, J., Bird, M. I., O'Brien, J. J., & McGuire, D. (2019). Groundwater-derived CO_2 dominates stream emissions across a tropical rainforest catchment. *Water Resources Research*, *55*(7), 4609–4623. https://doi.org/10.1029/2018WR024003

Emerson, S., & Hedges, J. I. (2008). *Chemical oceanography and the marine carbon cycle*. Cambridge University Press.

Gaucher, Y., Tanaka, K., Johansson, D. J. A., Goll, D. S., & Ciais, P. (2025). Leveraging ecosystems responses to enhanced rock weathering in mitigation scenarios. *Nature Communications*, *16*(1), 3021. https://doi.org/10.1038/s41467-025-58284-6

Godsey, S. E., Kirchner, J. W., & Clow, D. W. (2009). Concentration–discharge relationships reflect chemostatic characteristics of US catchments. *Hydrological Processes*, *23*(13), 1844–1864. https://doi.org/10.1002/hyp.7315

Horgby, Å., Segatto, P. L., Bertuzzo, E., Lauerwald, R., Lehner, B., Ulseth, A. J., et al. (2019). Unexpected large evasion fluxes of carbon dioxide from turbulent streams draining the world's mountains. *Nature Communications*, *10*(1), 4888. https://doi.org/10.1038/s41467-019-12905-z

Köhler, P., Hartmann, J., & Wolf-Gladrow, D. A. (2016). Enhanced weathering strategies for stabilizing climate and averting ocean acidification. *Nature Climate Change*, *6*(4), 402–406. https://doi.org/10.1038/nclimate2882

Lauerwald, R., Laruelle, G. G., Hartmann, J., Ciais, P., & Regnier, P. A. (2015). Spatial patterns in CO_2 evasion from the global river network. *Global Biogeochemical Cycles*, *29*(5), 534–554. https://doi.org/10.1002/2014GB004941

Lehmann, N., Lantuit, H., Böttcher, M. E., Hartmann, J., Eulenburg, A., & Thomas, H. (2023). Alkalinity generation from carbonate weathering in a silicate-dominated headwater catchment at Iskorasfjellet, northern Norway. *Biogeosciences*, *20*(16), 3459–3479. https://doi.org/10.5194/bg-20-3459-2023

Lupon, A., Peñarroya, X., Jativa, C., Xinyue, Z., Martí, E., & Catalán, N. (2025). *Confluences act as biogeochemical hot spots in mediterranean stream networks (Tech. Rep.)*. Copernicus Meetings. https://doi.org/10.5194/egusphere-egu25-8520

Maher, K., & Chamberlain, C. P. (2014). Hydrologic regulation of chemical weathering and the geologic carbon cycle. *Science*, *343*(6178), 1502–1504. https://doi.org/10.1126/science.1250770

Middelburg, J. J., Soetaert, K., & Hagens, M. (2020). Ocean alkalinity, buffering and biogeochemical processes. *Reviews of Geophysics*, *58*(3), e2019RG000681. https://doi.org/10.1029/2019RG000681

Millero, F. J. (1995). Thermodynamics of the carbon dioxide system in the oceans. *Geochimica et Cosmochimica Acta*, *59*(4), 661–677. https://doi.org/10.1016/0016-7037(94)00354-O

Raymond, P. A., Hartmann, J., Lauerwald, R., Sobek, S., McDonald, C., Hoover, M., et al. (2013). Global carbon dioxide emissions from inland waters. *Nature*, *503*(7476), 355–359. https://doi.org/10.1038/nature12760

Regnier, P., Resplandy, L., Najjar, R. G., & Ciais, P. (2022). The land-to-ocean loops of the global carbon cycle. *Nature*, *603*(7901), 401–410. https://doi.org/10.1038/s41586-021-04339-9

Rocher-Ros, G., Gomez-Gener, L., Jativa, C., Lannergård, E. E., Laudon, H., Lupon, A., et al. (2025). Emerging patterns of CO_2:O_2 dynamics in rivers and their link to ecosystem carbon processing. *Limnology and Oceanography Letters*, *10*(6), 835–850. https://doi.org/10.1002/lol2.70057

Saccardi, B., Brinkerhoff, C. B., Gleason, C. J., & Winnick, M. J. (2024). Toward modeling continental-scale inland water carbon dioxide emissions. *AGU Advances*, *5*(6), e2024AV001294. https://doi.org/10.1029/2024AV001294

Shangguan, Q., DeGrandpre, M. D., Hall Jr, R. O., & Payn, R. A. (2025). Freshwater carbonate buffering revisited. *Limnology and Oceanography Letters*, *10*(5), 619–635. https://doi.org/10.1002/lol2.70047

Shangguan, Q., Lai, C.-Z., Beatty, C. M., Young, F. L., Spaulding, R. S., & DeGrandpre, M. D. (2021). Autonomous in situ measurements of freshwater alkalinity. *Limnology and Oceanography: Methods*, *19*(2), 51–66. https://doi.org/10.1002/lom3.10404

Shangguan, Q., Payn, R. A., Hall Jr, R. O., Young, F. L., Valett, H. M., & DeGrandpre, M. D. (2024). Divergent metabolism estimates from dissolved oxygen and inorganic carbon: Implications for river carbon cycling. *Limnology and Oceanography*, *69*(9), 2211–2228. https://doi.org/10.1002/lno.12666

Stets, E. G., Butman, D., McDonald, C. P., Stackpoole, S. M., DeGrandpre, M. D., & Striegl, R. G. (2017). Carbonate buffering and metabolic controls on carbon dioxide in rivers. *Global Biogeochemical Cycles*, *31*(4), 663–677. https://doi.org/10.1002/2016GB005578

Wilcock, R. J., & Chapra, S. C. (2005). Diel changes of inorganic chemistry in a macrophyte-dominated, softwater stream. *Marine and Freshwater Research*, *56*(8), 1165–1174. https://doi.org/10.1071/MF05049

Winnick, M. J., & Saccardi, B. (2024). Impacts of carbonate buffering on atmospheric equilibration of CO_2, $\delta^{13}C_{DIC}$, and $\delta^{14}C_{DIC}$ in rivers and streams. *Global Biogeochemical Cycles*, *38*(2), e2023GB007860. https://doi.org/10.1029/2023GB007860

Wolf-Gladrow, D. A., Zeebe, R. E., Klaas, C., Körtzinger, A., & Dickson, A. G. (2007). Total alkalinity: The explicit conservative expression and its application to biogeochemical processes. *Marine Chemistry*, *106*(1–2), 287–300. https://doi.org/10.1016/j.marchem.2007.01.006

Zeebe, R. E., & Wolf-Gladrow, D. A. (2001). *CO2 in seawater: Equilibrium, kinetics, isotopes* (Vol. 65). Elsevier.